Cryogenics 162 (2026) 104466

Contents lists available at ScienceDirect

Cryogenics

journal homepage: www.elsevier.com/locate/cryogenics

# Selecting the minimum complexity for transient thermal-hydraulic modeling of HTS CICC at 20 K

Laura Savoldi [a,b,*], Martina Casciello [a,c], Mattia Gaspare Ciccarese [a], Mattia De Stasio [a,c], Michele Prisco [a], Andrea Tosin [d]

[a] Dipartimento Energia "Galileo Ferraris", Politecnico di Torino, Torino, Italy
[b] Istituto Nazionale di Fisica Nucleare, Sezione di Genova, Genova, Italy
[c] Istituto Nazionale di Fisica Nucleare, Sezione di Torino, Torino, Italy
[d] Dipartimento di Scienze Matematiche "Giuseppe Luigi Lagrange", Politecnico di Torino, Torino, Italy

## HIGHLIGHTS

- Thermal transients in HTS cable-in-conduit conductors are investigated.
- The minimum thermo-hydraulic model complexity is systematically assessed.
- The transition from 5 K to 20 K changes the dominant physics.
- Compressibility becomes secondary while diffusion remains important.
- A reduced advection-diffusion model preserves accuracy at low cost.

## ARTICLE INFO

*Keywords:*
HTS
CICC
Cryogenics
Thermal-hydraulics
Transient analysis
Reduced-order models

## ABSTRACT

The transition from low-temperature superconductors (LTS) operating at 4.5 K to high-temperature superconductors (HTS) at around 20 K represents a paradigm shift in fusion magnet design. This work investigates the minimum level of thermo-hydraulic model complexity required to accurately capture slow transient behavior in HTS Cable-In-Conduit Conductors (CICC) cooled by forced-flow helium. A complete thermal-hydraulic reference model is compared with progressively simplified advection and advection–diffusion models, where compressibility effects are incorporated through reduced-order formulations. The analysis focuses on energy transport and peak temperature prediction under representative operating conditions. Results show that, for slow transients, reduced-order models reproduce the key thermal features with acceptable accuracy while significantly reducing computational cost. The limits of validity of these simplifications are discussed with respect to compressibility effects and nonlinear material properties.

## 1. Introduction

Superconducting magnets operating at cryogenic temperatures are key enabling technologies for modern high-energy physics, fusion energy, and medical imaging applications. Their operation relies on maintaining the superconducting state under highly demanding thermal conditions, making the prediction of transient thermal behavior a crucial aspect of both design and safety analyses. Localized heat deposition events, such as particle losses, nuclear heating, or transient resistive phenomena, may lead to temperature excursions that reduce the available temperature margin and potentially trigger quenches.

High-temperature superconductors (HTS) are opening new perspectives for the design of next-generation fusion magnets by enabling operation at temperatures around 20 K, significantly above the conventional 4.5 K regime of low-temperature superconductors (LTS). This operating regime is being explored in several recent magnet developments, including those by Commonwealth Fusion Systems [1] and Energy Singularity Fusion Power Technology [2]. Among the conductor technologies considered for large-scale fusion applications, Cable-In-Conduit Conductors (CICCs) remain particularly attractive because of their efficient forced-flow helium cooling. For HTS CICCs, the transition

* Corresponding author at: Dipartimento Energia "Galileo Ferraris", Politecnico di Torino, Torino, Italy.
*Email address:* laura.savoldi@polito.it (L. Savoldi).

https://doi.org/10.1016/j.cryogenics.2026.104466
Received 20 June 2026; Received in revised form 11 August 2026; Accepted 26 August 2026
Available online 1 September 2026

to 20 K is not merely a change in operating temperature; rather, it fundamentally modifies the thermohydraulic response of the conductor.

Superconducting magnets in particle accelerators, such as the Large Hadron Collider at CERN [3], and fusion devices, such as ITER [4], operate under highly variable thermal loads arising from particle interactions, beam losses, nuclear heating, and transient electromagnetic effects. Cooling is typically provided by forced-flow helium circuits whose thermophysical properties strongly depend on temperature and pressure. The characteristic timescales of the resulting thermal transients range from milliseconds to hundreds of seconds [5,6], making both fluid transport and heat diffusion potentially relevant. Accurate prediction of conductor temperatures is therefore essential to guarantee operation below the critical temperature ($T_c$) of the superconducting material.

The thermal-hydraulic behavior of LTS CICCs has been extensively investigated over the last decades using detailed formulations based on the conservation equations of mass, momentum, and energy. Early approaches were developed using Euler-like formulations written in terms of velocity, pressure, and enthalpy [7], and later reformulated using non-conservative variables such as velocity, pressure, and temperature. These formulations constitute the basis of well-established simulation tools including Gandalf [8,9], SuperMagnet [10], OLYMPE [11], Mithrandir [12], M&M [13], 4C [14], and more recently OPENSC$^2$ [15]. Such tools have been extensively employed for the analysis of model coils, including the ITER Toroidal Field Model Coil [16–18] and the Central Solenoid Model Coil [19], for the interpretation of operational anomalies in devices such as KSTAR [20,21] and EAST [22], and for the design of future fusion magnets for DEMO [23–26] and CFETR [27]. Detailed thermal-hydraulic models have also been successfully applied to investigate both normal operating conditions [20,28] and off-normal scenarios, including quench events [29–32] and Loss-of-Flow accidents [33].

At 4.5 K, the transient thermal response is strongly governed by supercritical helium, whose large density variations and highly non-linear thermophysical properties play a dominant role in the evolution of the thermal field. By contrast, at temperatures around 20 K helium behaves essentially as a gas, while the dominant thermal inertia progressively shifts toward the solid components of the conductor, namely the jacket, copper stabilizer, and HTS stacks. This observation suggests that a significant fraction of the thermo-hydraulic complexity required in the LTS regime may become unnecessary in the HTS operating range.

Despite the extensive literature devoted to detailed thermal-hydraulic modeling of LTS conductors, considerably less attention has been devoted to understanding how much of this complexity remains necessary at 20 K. Simplified approaches have been proposed for specific applications, particularly for fast quench-oriented analyses and protection studies. An example is the CiccStream model developed for JT-60SA TF coils [34], which provides an efficient description of rapid off-normal events in LTS conductors. However, such formulations are typically tailored to specific accident scenarios and conductor configurations.

The present work addresses a different question. Rather than developing another application-specific simplified model, the objective is to identify the minimum level of thermo-hydraulic complexity required to accurately reproduce slow thermal transients in HTS CICCs operating around 20 K. To this end, a complete thermal-hydraulic reference formulation is systematically compared with a hierarchy of progressively simplified models. The comparison makes it possible to establish which physical mechanisms remain essential in the change of operating temperature and which can be consistently neglected without compromising predictive capability. When the transition from 4.5 K to 20 K is regarded as a transition between two distinct thermo-hydraulic regimes rather than as a simple change in operating temperature, the proposed methodology provides not only a reduced-order modeling strategy, but also a physics-based framework for identifying the hierarchy of the dominant mechanisms governing thermal transients in HTS cable-in-conduit conductors.

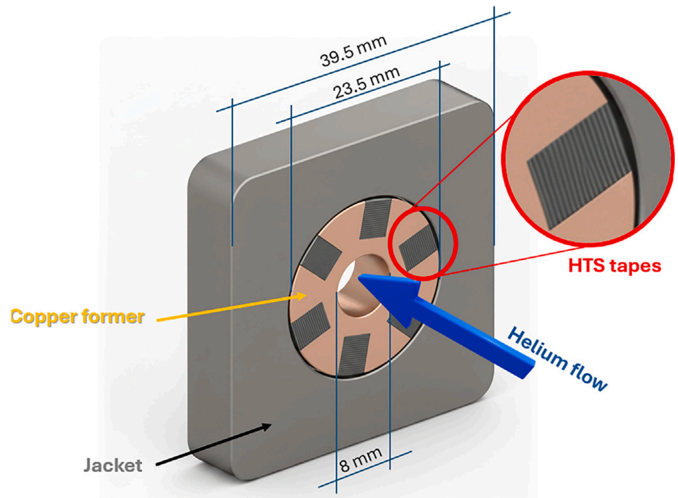


**Fig. 1.** Schematic representation of the CICC cross-section, including helium channel, copper–HTS region, and stainless-steel jacket.

## 2. Case study and methodology

### 2.1. Case study description

The analysis is carried out on a cable-in-conduit conductor (CICC) illustrated in Fig. 1, which could be representative of HTS fusion applications, as well as high-energy physics applications (see [35] for details). The conductor is composed of three main constituents: HTS stacks and copper stabilizer, a stainless-steel jacket, and forced-flow helium acting as the coolant.

To properly set up the thermal-hydraulic models investigated here, the physical measurements in Fig. 1 are translated into equivalent areas and wetted perimeters. These derived integral quantities, alongside the total cable length, are essential to accurately evaluate both the thermal inertia of each constituent and the heat transfer surfaces coupling them. Table 1 summarizes the calculated geometric properties based on the actual reference dimensions.

To broadly assess the minimum required complexity for the thermal-hydraulic models, two representative operating conditions are considered:

- Low-temperature regime (LTR, 5 K): fixed inlet mass flow rate of 5g/s, inlet and initial temperature of 5K, and outlet pressure of 5bar.

**Table 1**
Summary of the equivalent cross-sectional areas, wetted perimeters, heat transfer coefficients, friction factors, and total length implemented in the thermal-hydraulic models.

| Property | Symbol | Value | Unit |
|---|---|---|---|
| Helium channel cross section | $A_{He}$ | 50.27 | mm$^2$ |
| Helium-copper wetted perimeter | $P_{He,Cu}$ | 25.13 | mm |
| Copper-HTS region cross section | $A_{Cu}$ | 383.47 | mm$^2$ |
| Copper-SS wetted perimeter | $P_{Cu,SS}$ | 73.83 | mm |
| Stainless-steel jacket cross section | $A_{SS}$ | 1126.51 | mm$^2$ |
| Outer wetted perimeter | $P_{outer}$ | 158.00 | mm |
| Heat transfer coeff. (He-Cu) | $h_{He,Cu}$ | 1000 | W m$^{-2}$ K$^{-1}$ |
| Heat transfer coeff. (Cu-SS) | $h_{Cu,SS}$ | 500 | W m$^{-2}$ K$^{-1}$ |
| Laminar friction factor ($Re < 2300$) | $f_{laminar}$ | $64.0/Re$ | – |
| Turbulent friction factor ($Re \geq 2300$) | $f_{turbulent}$ | Haaland eq.* | – |
| Total cable length | $L$ | 167 | m |

* $f = \frac{1}{\left(-1.8\log_{10}\left[\left(\frac{\epsilon/D_h}{3.7}\right)^{1.11}+\frac{6.9}{Re}\right]\right)^2}$

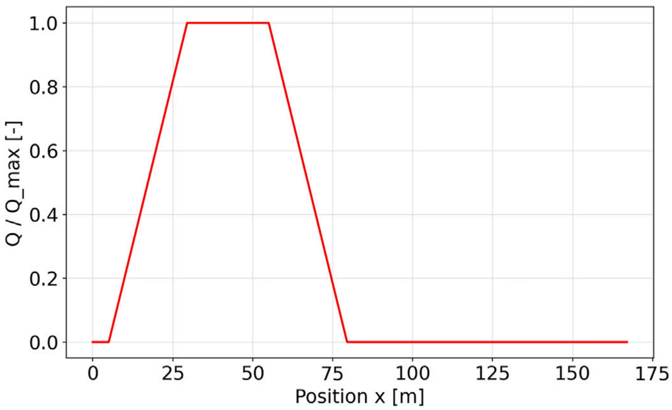


**Fig. 2.** Example of applied thermal load, suitably normalized. Heat load applied for $\tau_{load} = 100$ s.

- HTS operating regime (HTR, 20 K): fixed inlet mass flow rate of 5g/s, inlet and initial temperature of 20K, and outlet pressure of 20bar.

The transient is driven by an externally applied thermal load distributed along the cable, see for instance Fig. 2, which constitutes a simplified version of a realistic heat load spatial distribution [35].

The analysis focuses on representative operating scenarios rather than extreme conditions. In particular, the following cases are selected:

- **Case 1:** LTR with low temperature increase, with a temperature rise $\Delta T$ of approximately 2K, corresponding to the standard operation of LTS CICC for fusion magnets.
- **Case 2:** LTR, with high $\Delta T$ of approximately 8K, which could correspond to the operation of HTS CICC in fusion magnets, where the cryoplant should also feed magnets at 5 K.
- **Case 3:** HTR with high $\Delta T$ of approximately 8K, representative of HTS fusion-magnet operation and encompassing also lower-amplitude temperature excursions.

### 2.2. Assumptions and simplifications

The geometrical configuration is described in terms of equivalent cross-sectional areas associated with each component, allowing for a one-dimensional thermal-hydraulic representation along the cable axis. In fact, for slow transients, such as those associated with current ramp-up and ramp-down phases considered in [35], the HTS stacks and copper former can be treated as a single equivalent solid domain. To justify the single-temperature approximation adopted for the HTS stacks and copper stabilizer, the characteristic thermal equilibration timescale within the solid domain can be compared with the characteristic timescale of the applied transient.

The characteristic diffusion time in the solid can be estimated as:

$$\tau_{\text{solid}} \sim \frac{L_c^2}{\alpha_s}, \tag{1}$$

where ($L_c$) is the characteristic length of transverse diffusion and ($\alpha_s = \frac{k_s}{\rho_s c_{p,s}}$) is the thermal diffusivity of the equivalent solid domain.

Typical values for copper-stabilized HTS conductors are $\alpha_s \sim 10^{-3} - 10^{-2}\ \text{m}^2/\text{s}$, while the characteristic transverse length scale is of the order of a few millimeters. This leads to characteristic thermal equilibration times ranging approximately from $10^{-3}$ s to $10^{-1}$ s.

By contrast, the thermal loads considered in the present work evolve over characteristic timescales of the order of ($10^2$, s). Therefore:

$$\tau_{\text{solid}} \ll \tau_{\text{load}} \tag{2}$$

**Table 2**
Thermal diffusion characteristic times.

| Material | $\tau_{\text{diff}}$ [s] @ 5 K | $\tau_{\text{diff}}$ [s] @ 20 K |
|---|---|---|
| He | $2 \times 10^{-3}$ | $8.44 \times 10^{-4}$ |
| Cu | $1.47 \times 10^{-3}$ | $2.2 \times 10^{-2}$ |
| SS | 6.15 | 4.66 |

indicating that thermal equilibrium between the HTS stacks and the copper stabilizer is established much faster than the transient evolution itself. This strong separation of timescales justifies the use of a single equivalent temperature for the HTS-copper domain in the reduced-order models.

The characteristic thermal response time of helium can be estimated as:

$$\tau_{\text{He}} = \frac{\rho_{\text{He}} c_{p,\text{He}} A_{\text{He}}}{h_{\text{conv}} P} \tag{3}$$

For all the cases considered, it is found that:

$$\tau_{\text{He}} \ll \Delta t_{\text{load}} \tag{4}$$

which validates the assumption of *slow transient* conditions. Under this assumption, the system response is governed by the gradual evolution of the thermal field rather than by fast local equilibration processes.

Table 2 shows the characteristic thermal diffusion times for helium, copper, and stainless steel at 5 K and 20 K. The results indicate that thermal equilibration in helium and copper occurs on very short timescales, on the order of $10^{-3}$–$10^{-2}$ s, while the stainless steel domain exhibits significantly slower diffusion dynamics, with characteristic times of several seconds. Even the largest diffusion timescale, associated with the stainless-steel jacket, remains at least one order of magnitude smaller than the characteristic transient duration considered in this work. Therefore, all the estimated diffusion times remain significantly shorter than the characteristic timescale of the applied thermal loads, confirming a strong separation of timescales and supporting the assumption of quasi-steady thermal equilibrium within the conductor cross-section during the transient evolution. This separation of timescales is also a key condition for the validity of the reduced-order models introduced in Section 3.

### 2.3. Methodology

The methodology adopted in this work is based on a systematic comparison between models of increasing levels of simplification.

The procedure consists of the following steps:

1. The transient behavior is first evaluated using the reference thermal-hydraulic model (Model “REF”), which includes the full set of Euler-like equations and represents the most accurate description under the selected operating conditions.
2. A coupled advection–diffusion model (Model “AD1”) is then analyzed. In this model, the operating conditions are adjusted to include the effects of velocity variation and compressibility through reduced-order formulations.
3. A single-equation thermal advection–diffusion model (Model ”AD2”) is developed. In this model, a single equation is used for the average cable temperature, while velocity variations and compressibility effects are included through reduced-order formulations.
4. Finally, the pure advection model (Model “PA”) is considered, again with appropriate adjustments to account for pressure effects in a simplified manner.

The comparison between these models is carried out in terms of average temperature evolution, transported energy, and peak temperature values. This systematic approach allows us to assess whether the simplified models are capable of reproducing the key physical features of the transient while significantly reducing computational complexity.

## 3. Numerical models

In this section, the different modeling approaches adopted in this work are presented, ranging from a complete thermal-hydraulic formulation to progressively simplified models. All models are formulated in one-dimensional form along the conductor axis.

### 3.1. Reference thermal-hydraulic model

The reference model (labelled "REF") describes the coupled evolution of helium flow and solid temperatures through a set of mass, momentum, and energy equations, including temperature- and pressure-dependent properties.

*Helium governing equations.* We consider the well-established set of Euler-like equations written in terms of the non-conservative variables helium velocity, pressure, and temperature, denoted by $v$, $p$, and $T$, respectively, as derived from the standard conservation laws:

$$\frac{\partial v}{\partial t} + v\frac{\partial v}{\partial x} + \frac{1}{\rho_{\mathrm{He}}}\frac{\partial p}{\partial x} = -\frac{2fv|v|}{D_h} \tag{5}$$

$$\frac{\partial p}{\partial t} + \rho_{\mathrm{He}}c_{\mathrm{He}}^2\frac{\partial v}{\partial x} + v\frac{\partial p}{\partial x} = \phi_{\mathrm{He}}\left(\frac{h_{\mathrm{He,Cu}}P_{\mathrm{He,Cu}}}{A_{\mathrm{He}}}\left(T_{\mathrm{Cu}} - T_{\mathrm{He}}\right) + \frac{2\rho_{\mathrm{He}}fv^3}{D_h}\right) \tag{6}$$

$$\frac{\partial T_{\mathrm{He}}}{\partial t} + v\frac{\partial T_{\mathrm{He}}}{\partial x} + \phi_{\mathrm{He}}T_{\mathrm{He}}\frac{\partial v}{\partial x} = \frac{1}{\rho_{\mathrm{He}}c_{v,\mathrm{He}}}\left(\frac{h_{\mathrm{He,Cu}}P_{\mathrm{He,Cu}}}{A_{\mathrm{He}}}\left(T_{\mathrm{Cu}} - T_{\mathrm{He}}\right) + \frac{2\rho_{\mathrm{He}}fv^3}{D_h}\right) \tag{7}$$

where $\rho_{\mathrm{He}}$, $c_{\mathrm{He}}$ and $c_{v,\mathrm{He}}$ denote the helium density, sound speed and specific heat at constant volume, respectively. In all equations, the flow resistance and the associated heat generation are governed by the friction term, which depends on the hydraulic diameter of the channel ($D_h$) and the Fanning friction factor ($f$).

The term $\phi_{\mathrm{He}}$ denotes the Grüneisen parameter, which characterizes the coupling between thermal and mechanical effects in helium. A larger value of $\phi_{\mathrm{He}}$ corresponds to a stronger influence of heating on the pressure-driven dynamics of the fluid, making this term particularly important during compressible transients. Finally, it must be emphasized that the helium thermophysical properties ($\rho_{\mathrm{He}}$, $c_{\mathrm{He}}$, $c_{v,\mathrm{He}}$, and $\phi_{\mathrm{He}}$) are strongly nonlinear functions of the local pressure and temperature.

*Solid domain.* The solid components (copper-HTS region with index Cu and stainless steel region with index SS) are treated separately by means of the following equations:

$$A_{\mathrm{SS}}\rho_{\mathrm{SS}}c_{p,\mathrm{SS}}\frac{\partial T_{\mathrm{SS}}}{\partial t} = A_{\mathrm{SS}}\frac{\partial}{\partial x}\left(k_{\mathrm{SS}}\frac{\partial T_{\mathrm{SS}}}{\partial x}\right) + h_{\mathrm{Cu,SS}}P_{\mathrm{Cu,SS}}\left(T_{\mathrm{Cu}} - T_{\mathrm{SS}}\right) \tag{8}$$

$$A_{\mathrm{Cu}}\rho_{\mathrm{Cu}}c_{p,\mathrm{Cu}}\frac{\partial T_{\mathrm{Cu}}}{\partial t} = A_{\mathrm{Cu}}\frac{\partial}{\partial x}\left(k_{\mathrm{Cu}}\frac{\partial T_{\mathrm{Cu}}}{\partial x}\right) - \sum_{i\in\{\mathrm{He,SS}\}} h_{i,\mathrm{Cu}}P_{i,\mathrm{Cu}}\left(T_{\mathrm{Cu}} - T_i\right) + q', \tag{9}$$

where $\rho$, $c_p$, and $k$ designate the density, specific heat, and thermal conductivity of the respective solid materials. Both the specific heat and the thermal conductivity are evaluated as strictly temperature-dependent properties. The term $q'$ represents the linear heat generation rate applied to the conductor, which accounts for the AC losses driving the transient according to the selected operating regime (LTR or HTR).

To close the system of equations, boundary and initial conditions are specified according to the selected operating regime (LTR or HTR). Regarding the solid domains, adiabatic boundary conditions are imposed at both ends ($x = 0$ and $x = L$) for the equivalent copper-HTS region and the stainless-steel jacket:

$$\left.\frac{\partial T_{\mathrm{Cu}}}{\partial x}\right|_{x=0,L} = 0, \quad \left.\frac{\partial T_{\mathrm{SS}}}{\partial x}\right|_{x=0,L} = 0. \tag{10}$$

For the fluid domain, the helium inlet temperature $T_{op}$ and the outlet pressure $p_{op}$ are fixed to their nominal operating values (either 5 K and 5 bar for LTR, or 20 K and 20 bar for HTR). Furthermore, a constant inlet mass flow rate $\dot{m} = 5$ g/s is enforced by prescribing the inlet velocity:

$$T_{\mathrm{He}}(0,t) = T_{op}, \quad p_{\mathrm{He}}(L,t) = p_{op}, \quad v_{\mathrm{He}}(0,t) = \frac{\dot{m}}{\rho_{\mathrm{He}}(T_{op}, p_{op})A_{\mathrm{He}}}. \tag{11}$$

Finally, concerning the initial state, the system is assumed to be initially at thermal equilibrium, featuring a uniform temperature profile along the conductor corresponding to the reference operating temperature:

$$T_{\mathrm{He}}(x,0) = T_{\mathrm{Cu}}(x,0) = T_{\mathrm{SS}}(x,0) = T_{op}. \tag{12}$$

These values are representative of typical thermal coupling conditions in CICCs and allow for a consistent comparison between models.

### 3.2. Model AD1: coupled advection–diffusion model

Model AD1 retains separate equations for helium and solid domains, but simplifies the momentum equation and reduces the fluid description to an advection-dominated energy balance.

*Helium.*

$$c_{p,\mathrm{He}}\left(A_{\mathrm{He}}\rho_{\mathrm{He}}\frac{\partial T_{\mathrm{He}}}{\partial t} + \dot{m}\frac{\partial T_{\mathrm{He}}}{\partial x}\right) = h_{\mathrm{He,Cu}}P_{\mathrm{He,Cu}}\left(T_{\mathrm{Cu}} - T_{\mathrm{He}}\right) + q'_{\mathrm{fric}} \tag{13}$$

*Copper.*

$$A_{\mathrm{Cu}}\rho_{\mathrm{Cu}}c_{p,\mathrm{Cu}}\frac{\partial T_{\mathrm{Cu}}}{\partial t} = A_{\mathrm{Cu}}\frac{\partial}{\partial x}\left(k_{\mathrm{Cu}}\frac{\partial T_{\mathrm{Cu}}}{\partial x}\right) - \sum_{i\in\{\mathrm{He,SS}\}} h_{i,\mathrm{Cu}}P_{i,\mathrm{Cu}}\left(T_{\mathrm{Cu}} - T_i\right) + q' \tag{14}$$

*Stainless steel.*

$$A_{\mathrm{SS}}\rho_{\mathrm{SS}}c_{p,\mathrm{SS}}\frac{\partial T_{\mathrm{SS}}}{\partial t} = A_{\mathrm{SS}}\frac{\partial}{\partial x}\left(k_{\mathrm{SS}}\frac{\partial T_{\mathrm{SS}}}{\partial x}\right) + h_{\mathrm{Cu,SS}}P_{\mathrm{Cu,SS}}(T_{\mathrm{Cu}} - T_{\mathrm{SS}}) \tag{15}$$

The thermal transients are driven by specific heat sources: $q'_{\mathrm{fric}}$ accounts for the heat generated by fluid friction within the helium channel, while $q'$ represents the external heat load, such as AC losses, applied to the copper-HTS region. As in the previous formulation, the thermophysical properties of the materials are evaluated as temperature-dependent. Furthermore, compressibility effects are incorporated through a reduced-order formulation for the velocity (and, consequently, mass flow rate) variation in time and space, see below.

Model AD1 adopts the same thermal boundary and initial conditions as the full thermal-hydraulic reference model to ensure a consistent comparison. However, as we transition from a complete thermal-hydraulic description to a simplified model that does not directly solve all three conservation equations, relying solely on the energy conservation equation for the fluid, while velocity and pressure are handled via the reduced-order formulation, explicit hydrodynamic boundary conditions are no longer required.

The initial and boundary conditions are thus defined to reflect this simplified mathematical formulation. Regarding the solid domains, the equivalent copper-HTS region and the stainless-steel jacket remain strictly adiabatic at both the inlet ($x = 0$) and outlet ($x = L$) boundaries:

$$\left.\frac{\partial T_{\mathrm{Cu}}}{\partial x}\right|_{x=0,L} = 0, \quad \left.\frac{\partial T_{\mathrm{SS}}}{\partial x}\right|_{x=0,L} = 0. \tag{16}$$

For the fluid domain, because the explicit resolution of mass, momentum and energy conservation laws is dropped in favor of an advection-dominated energy balance, the helium flow only requires a prescribed inlet temperature, which is continuously fixed at the selected nominal operating value ($T_{op}$):

$$T_{\mathrm{He}}(0,t) = T_{op}. \tag{17}$$

Finally, concerning the initial state, the system is initialized from a uniform thermal steady-state, assuming perfect equilibrium across all components at the reference operating temperature:

$$T_{\mathrm{He}}(x,0) = T_{\mathrm{Cu}}(x,0) = T_{\mathrm{SS}}(x,0) = T_{op}. \tag{18}$$

### 3.3. Model AD2: single-equation advection–diffusion model

Model AD2 further simplifies the system by introducing a single equation for the mean temperature of the coupled solid–helium system, as derived in Appendix B:

$$(c_s + c_{\mathrm{He}})\frac{\partial T_{\mathrm{mean}}}{\partial t} + u_{\mathrm{eff}}\frac{\partial T_{\mathrm{mean}}}{\partial x} = \alpha_{\mathrm{eff}}\frac{\partial^2 T_{\mathrm{mean}}}{\partial x^2} + q' + q'_{\mathrm{fric}}, \tag{19}$$

where the equivalent heat capacities per unit length are defined as:

$$c_s = A_s \rho_s c_{p,s}, \quad c_{\mathrm{He}} = A_{\mathrm{He}} \rho_{\mathrm{He}} c_{p,\mathrm{He}} \tag{20}$$

$$u_{\mathrm{eff}} = \dot{m} c_{p,\mathrm{He}} \tag{21}$$

$$\alpha_{\mathrm{eff}} = A_s k_s + \frac{1}{2} c_{\mathrm{He}} u B \tag{22}$$

with:

$$B = \frac{u}{h_{\mathrm{He,Cu}} P_{\mathrm{He,Cu}} \left(\frac{1}{c_{\mathrm{He}}} + \frac{1}{c_s}\right)}. \tag{23}$$

The equivalent solid properties (identified by the index “s”) are computed through weighted averages of the copper and stainless-steel contributions. The equivalent solid heat capacity per unit length is obtained by summing the mass-averaged contributions of the individual solid constituents, whereas the effective axial thermal conductivity is area-weighted.

As defined in the previous models, the heat sources include the external AC losses and the fluid friction. It is crucial to note that both the solid equivalent properties and the helium thermophysical properties are evaluated strictly as nonlinear functions of the local temperature.

By reducing the coupled thermal system to a single advection-diffusion equation for the cable mean temperature, the initial and boundary conditions must be adapted to reflect this lumped representation. Since the fluid and solid domains are merged into a single equivalent medium, only one set of boundary conditions is required. Specifically, at the cable inlet ($x = 0$), the mean temperature is fixed to the selected reference operating value ($T_{op}$). Conversely, at the cable outlet ($x = L$), an adiabatic boundary condition is enforced on the mean temperature profile:

$$T_{\mathrm{mean}}(0,t) = T_{op}, \quad \left.\frac{\partial T_{\mathrm{mean}}}{\partial x}\right|_{x=L} = 0 \tag{24}$$

Consistently with the other models, the transient is initialized from a uniform steady-state condition, assuming the entire cable is at the nominal operating temperature:

$$T_{\mathrm{mean}}(x,0) = T_{op} \tag{25}$$

### 3.4. Model PA: pure advection model

The simplest model considered is obtained by neglecting diffusive effects, resulting in a pure advection equation for the mean temperature:

$$(c_s + c_{\mathrm{He}})\frac{\partial T_{\mathrm{mean}}}{\partial t} + u_{\mathrm{eff}}\frac{\partial T_{\mathrm{mean}}}{\partial x} = q'_{\mathrm{fric}}. \tag{26}$$

This model represents the limiting case in which both thermal diffusion and solid-fluid temperature differences are completely neglected.

The boundary and initial conditions for the pure advection (PA) model are tailored to its specific mathematical nature. Since the formulation relies on a first-order spatial derivative, it requires only a single boundary condition. Therefore, the mean temperature at the cable inlet ($x = 0$) is simply fixed to the reference operating value ($T_{op}$):

$$T_{\mathrm{mean}}(0,t) = T_{op}. \tag{27}$$

Regarding the initial state, because the PA model lacks the diffusive terms necessary to simulate localized heat deposition dynamically, the initial temperature distribution $T_{\mathrm{mean}}(x,0)$ is forced to follow a normalized shape that mirrors the spatial distribution of the applied heat load. The rigorous determination of this initial temperature profile, which ensures the conservation of the total deposited energy through an iterative enthalpy balance, is detailed in Appendix C.

### 3.5. Continuity equation

In the simplified advection and advection-diffusion models, the explicit resolution of the momentum conservation equation is bypassed to significantly reduce computational complexity. However, during thermal transients, helium undergoes strong thermal expansion, leading to fluid velocity variations driven by compressibility. To accurately account for these fluid dynamics without relying on complex and potentially unstable pressure ordinary differential equations (ODEs), a lumped spatial formulation based on the continuity equation is employed.

This approach, which can be described as a quasi-compressible or “Low-Mach” approximation, starts from the standard one-dimensional mass conservation equation:

$$\frac{\partial \rho_{\mathrm{He}}}{\partial t} + \frac{\partial(\rho_{\mathrm{He}} v)}{\partial x} = 0. \tag{28}$$

Rather than solving a tightly coupled momentum-pressure system, this relationship dictates that the mass flow rate, and consequently the local velocity, change along the conductor strictly as a function of the temporal variation of the helium density.

The primary strength of this strategy lies in its self-contained and explicitly decoupled nature: it requires no hydrodynamic information or closure variables beyond the evolution of the temperature field itself. Numerically, the energy equations for the cable temperatures are solved first, using the mass flow rates from the previous time step. These newly updated temperatures are then used to evaluate the local helium density and its temporal variation. By integrating this density derivative along the spatial coordinate and applying the prescribed inlet mass flow rate, the updated mass flow rate profile $\dot{m}(x)$ is obtained directly.

Once the mass flow rate distribution is determined, the local fluid velocity $v(x)$ is explicitly recovered at each spatial location according to its algebraic definition:

$$v(x) = \frac{\dot{m}(x)}{\rho_{\mathrm{He}}(x) A_{\mathrm{He}}}, \tag{29}$$

where $A_{\mathrm{He}}$ is the cross-sectional area of the helium channel. As detailed in Appendix A, this sequential formulation completely eliminates the need for iterative pressure solvers while robustly preserving the essential physics of fluid expansion.

## 4. Numerics

The system of governing equations is numerically solved by applying the finite difference method (FDM) over a uniform 1D staggered grid. To guarantee numerical stability and mitigate spurious oscillations in the presence of strong convective transport, the advective terms are discretized using a second-order upwind scheme. Conversely, the conductive and diffusive terms are approximated via second-order centered finite differences to preserve spatial accuracy.

Time integration is performed employing a fully implicit Euler method, which ensures unconditional stability even for large integration steps. The highly nonlinear physical properties of supercritical helium and the solid domains are handled using a frozen coefficient approach; specifically, the material properties and heat transfer coefficients are evaluated explicitly based on the thermodynamic state of the previous time step, effectively linearizing the system matrix for the current iteration. At the domain extremities, the boundary conditions are strictly enforced using first-order forward and backward difference schemes.

For all the transient scenarios investigated in this study, the computational domain has been discretized using a uniform spatial grid with $\Delta x = 0.5$ m and a fixed time step of $\Delta t = 0.5$ s. This specific spatio-temporal discretization was rigorously selected to ensure a grid-independent solution while maintaining an acceptable overall computational cost for the extensive batch analyses.

## 5. Results

### 5.1. Reference model behavior

For the reference model, the mean (weighted average) temperature is defined as:

$$T_{\text{avg}} = \frac{\sum_i A_i \rho_i c_{p,i} T_i}{\sum_i A_i \rho_i c_{p,i}}, \quad i \in \{\text{He}, \text{Cu}, \text{SS}\}. \tag{30}$$

The reference model exhibits strong nonlinear effects, including steep thermal gradients and the propagation of complex thermal fronts. As shown in Fig. 3, the thermal response heavily depends on the operating temperature. In the low-temperature regimes (5 K, Fig. 3a and b), the temperature profile develops a distinct asymmetry. As the heat load increases (Case 2), the rapid expansion of the supercritical helium pushes the thermal wave downstream, creating a steeper front and an elongated tail. Conversely, in the 20 K regime (Fig. 3c), the thermal wave propagates with a much more symmetric, Gaussian-like shape, reflecting the dominant thermal inertia of the solid components and the reduced influence of helium expansion.

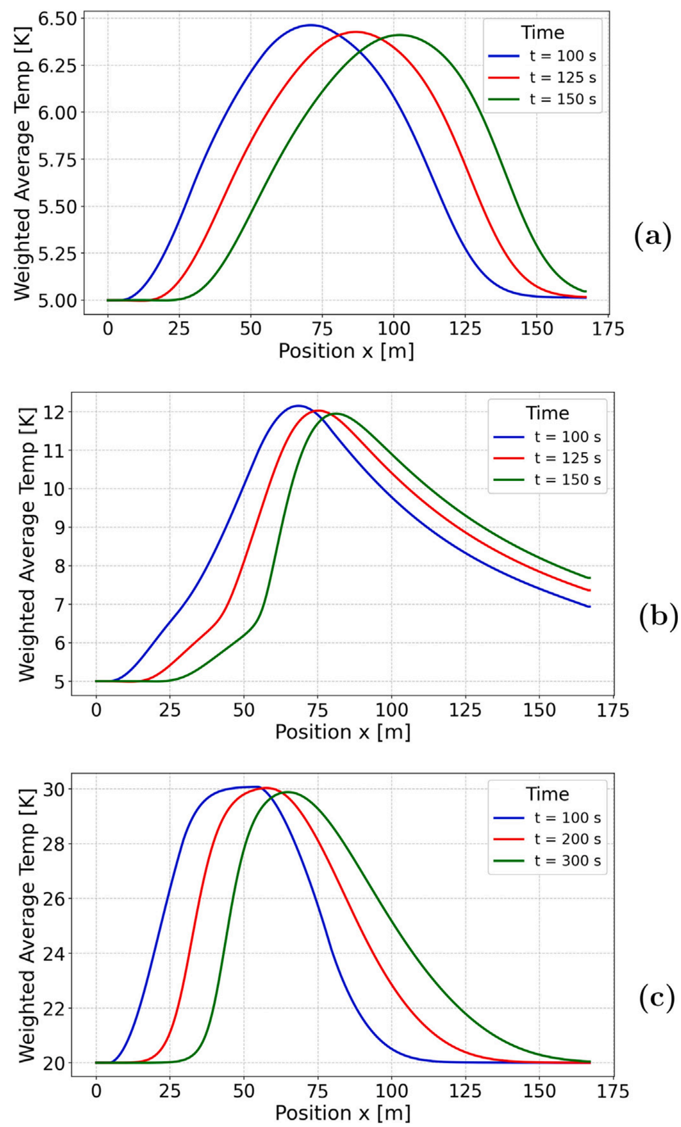


**Fig. 3.** Profiles of the weighted average temperature $T_{\text{avg}}$ predicted by the reference thermal-hydraulic model at the selected times for the three operating cases: (a) Case 1; (b) Case 2; (c) Case 3.

### 5.2. Comparison with reduced models

#### 5.2.1. Advection-diffusion models

Considering first the low-temperature cases shown in Fig. 4(a) and (b), good overall agreement is observed among the models. However, small discrepancies are found both in the peak temperature, up to approximately 0.2 K, and in the shape of the temperature profiles. The simplified models tend to underestimate the peak values at the lowest heat loads (Case 1), whereas a slight overestimation is observed at higher thermal loads (Case 2), for which the trailing edge of the thermal wave is also not perfectly captured. Simplifying the momentum equation therefore introduces minor discrepancies when dealing with the strong pressure variations of helium at 5 K. By contrast, very good agreement is observed at 20 K (Fig. 4c), where the simplified models closely reproduce both the peak magnitude and the spatial distribution predicted by the reference model.

#### 5.2.2. Pure advection model

The limitations of entirely neglecting thermal diffusion are highlighted in Fig. 5. The pure advection (PA) model fails significantly at low temperatures (Fig. 5a and b), overpredicting the maximum temperature and causing an unphysical, sharp localization of the heat wave that severely lags behind the actual spatial peak. At 20 K (Fig. 5c), the PA model provides more reasonable temperature amplitude results, but it still suffers from spatial delays and a lack of the natural smoothing provided by solid conduction, resulting in artificially steep gradients.

### 5.3. Effect of compressibility

Fig. 6 isolates the impact of fluid compressibility, demonstrating why it is critical at low temperatures and negligible at 20 K. As seen in Fig. 6(a), a transient at 5 K causes the normalized helium velocity to spike dramatically—up to five times the initial velocity for high $\Delta T$ cases—driven by intense localized thermal expansion. This expansion simultaneously produces a strong local variation of the mass flow rate (Fig. 6a, right axis). If these compressibility effects are ignored at 5 K (constant mass flow assumption), an unacceptable temperature deviation exceeding 4 K is induced, as shown in Fig. 7(a). By contrast, at 20 K, helium behaves like a gas; velocity spikes are minimal, mass flow remains stable, and neglecting compressibility introduces only minor deviations in the temperature field (Fig. 7b).

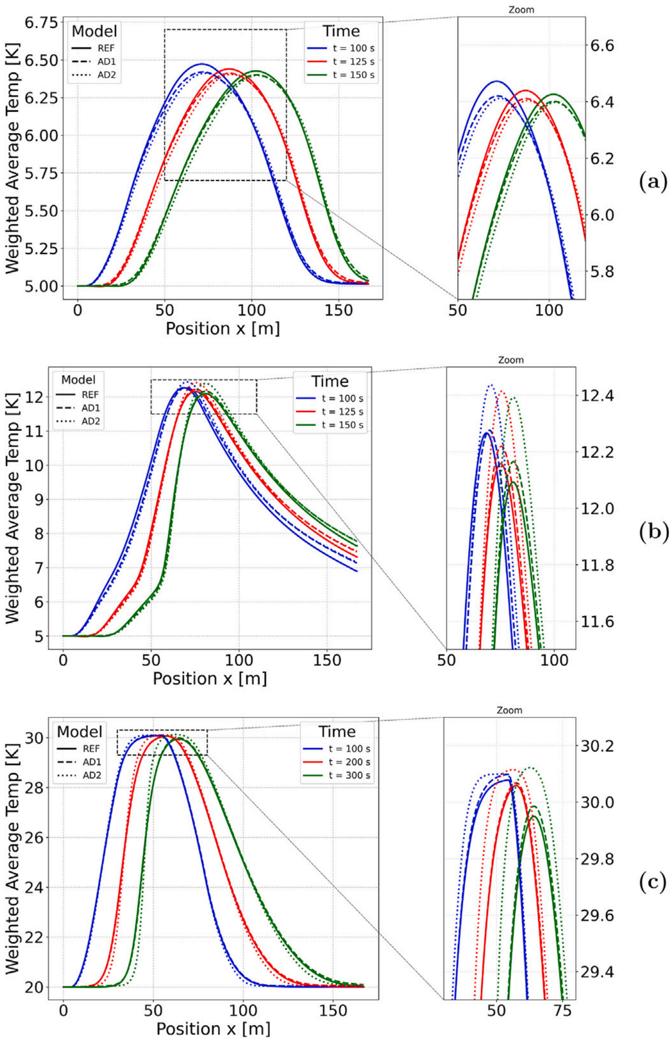


**Fig. 4.** Comparison of the profiles of the weighted average temperature $T_{avg}$ predicted by the reference (REF) and AD1 models and of the $T_{mean}$ computed with the AD2 model at the selected times for the three operating cases: (a) Case 1; (b) Case 2; (c) Case 3.

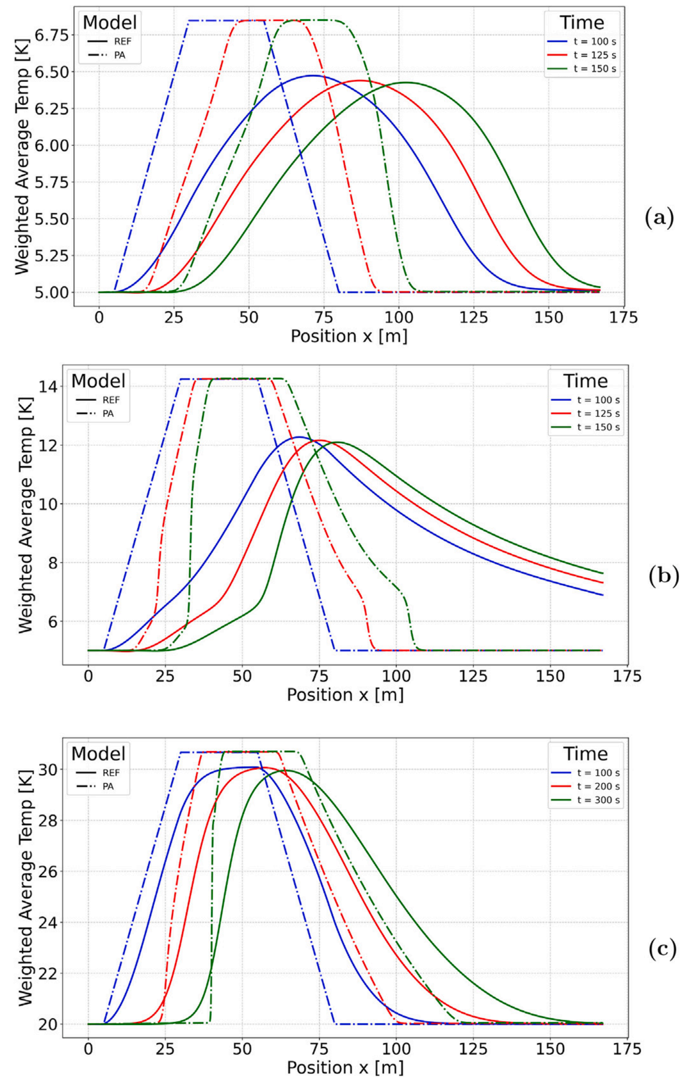


**Fig. 5.** Comparison of the profiles of the weighted average temperature $T_{avg}$ predicted by the reference (REF) model and of the temperature computed with the pure-advection (PA) model at the selected times for the three operating cases: (a) Case 1; (b) Case 2; (c) Case 3.

## 6. Discussion

The various numerical models, characterized by substantially different levels of physical and mathematical simplification, exhibit different computational performances. To ensure a rigorous and fair benchmark, the measured CPU times reported in this section strictly isolate the core algorithmic effort: the assembly of the sparse matrices and the linear system inversion. Overheads related to non-linear thermodynamic property updates, external database calls, and data I/O exports have been explicitly excluded. Furthermore, all simulations compared in this benchmark were executed using an identical spatial and temporal discretization ($\Delta x = 0.5\,\mathrm{m}$ and $\Delta t = 0.5\,\mathrm{s}$). Finally, while the reduced-order models (PA, AD1, AD2) are implemented in MATLAB and the reference model (REF) in Python (`scipy.sparse`), both environments internally rely on highly optimized C/Fortran backends for linear algebra, thereby limiting implementation-dependent differences and supporting a meaningful comparison of the core algorithmic cost.

As illustrated in Fig. 8, reducing the number of governing equations leads to a substantial decrease in computational cost. The PA model is the fastest, but this advantage is accompanied by large discrepancies with respect to the reference solution, see also below. AD1 and AD2 provide a more favorable compromise between computational cost and physical accuracy.

Finally, comparing the compressible (solid bars) and incompressible (hatched bars) variants of the reduced models reveals that the performance difference is generally minimal. Since the lumped compressibility approach merely requires an additional spatial integration step for the continuity equation, its direct computational overhead is extremely small. The minor variations in execution time observed are often driven by how the thermal expansion alters the fluid velocity, which in turn slightly modifies the diagonal conditioning of the sparse matrix, making the linear system marginally faster or slower to invert.

It should be stressed that the practical relevance of this computational reduction depends on the intended use of the model. For a single analysis of a unique conductor configuration, the numerical solution time may represent only a limited fraction of the overall engineering effort, which also includes model preparation, verification, sensitivity assessment, and interpretation of the results. The reduced-order formulations are therefore not intended to replace the complete thermal-hydraulic model indiscriminately in every R&D application. Their main advantage arises once their validity has been established for a given class of conductors and operating conditions and a large

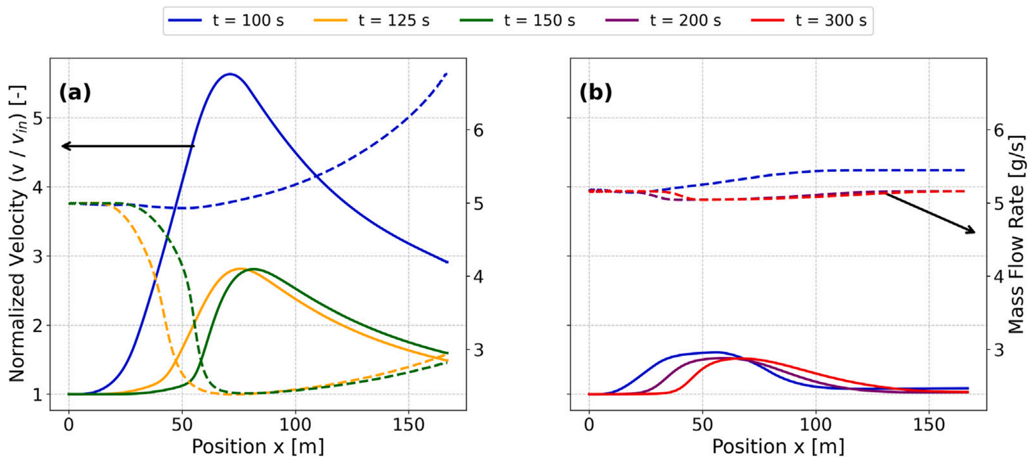


**Fig. 6.** Normalized helium velocity (solid lines, left axis) and mass flow rate (dashed lines, right axis) along the conductor, illustrating the effect of compressibility for: (a) Case 2; (b) Case 3.

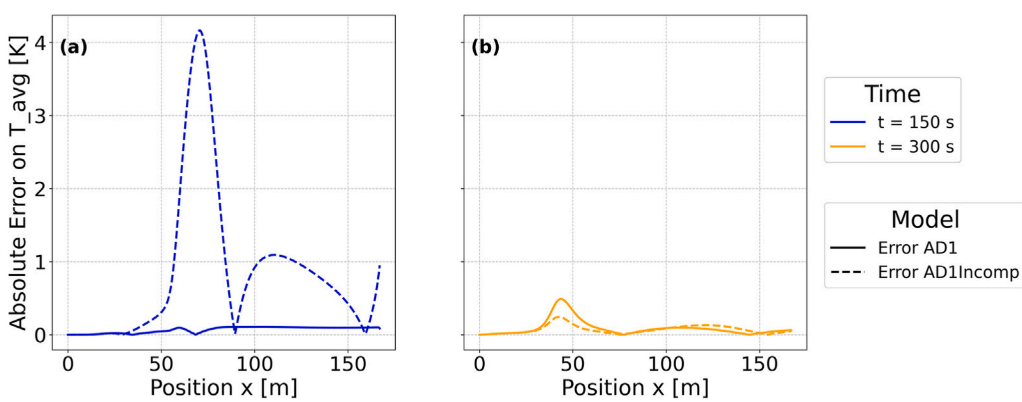


**Fig. 7.** Absolute deviation of the weighted average temperature $T_{avg}$ caused by neglecting compressibility in the AD1 model: (a) Case 2; (b) Case 3.

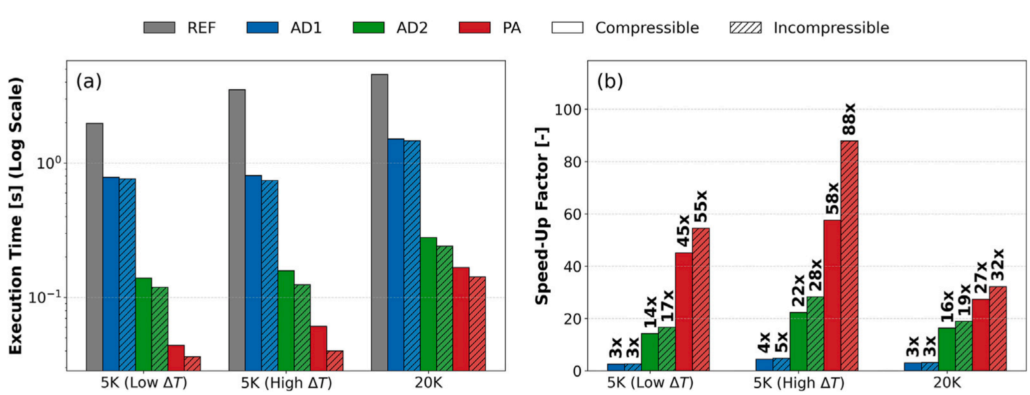


**Fig. 8.** Comparison of the computational performance of the investigated models: (a) execution time of the core solver on a logarithmic scale; (b) speed-up factor relative to the reference (REF) model.

number of closely related simulations is required. Typical examples include parametric and sensitivity studies, uncertainty analyses, design optimization, repeated operating-scenario evaluations, and coupled magnet–cryogenic-network simulations. In such applications, the cumulative computational cost may become substantial, and the reduction achieved by AD2 allows a considerably broader exploration of the design and operating space. A practical use of the proposed model hierarchy can therefore rely on a two-level strategy: the REF formulation is employed for selected reference or bounding cases to establish the range of validity of the reduced description, whereas AD2 can subsequently be used for repeated calculations within the validated operating domain.

To quantitatively assess the performance of the simplified models compared to the complete thermal-hydraulic reference formulation, several Key Performance Indicators (KPIs) are defined. This rigorous validation is essential for evaluating the applicability of reduced-order models in the design of next-generation high-temperature superconducting (HTS) devices. The analysis specifically focuses on the maximum mean temperature ($T_{max}$) and its spatial location ($x_{max}$) at the end of the heat deposition phase.

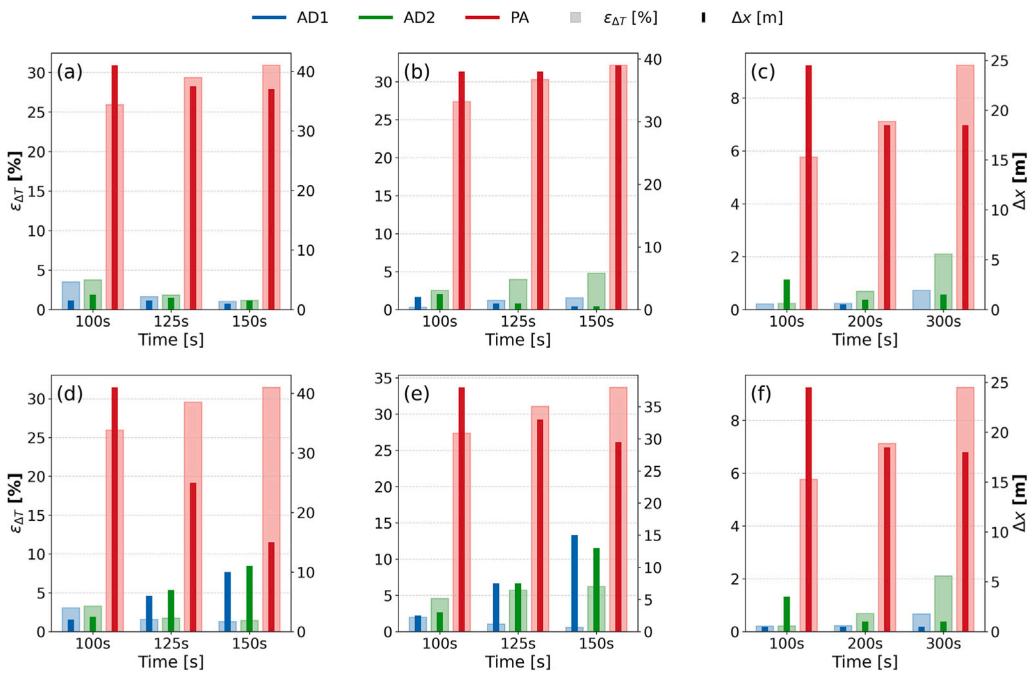


**Fig. 9.** Comparison of the key performance indicators (KPIs) for the investigated models. The left axis reports the relative error in the peak temperature, whereas the right axis reports the absolute error in the peak position. The upper row refers to the compressible models and the lower row to the incompressible models: (a,d) Case 1; (b,e) Case 2; (c,f) Case 3.

The accuracy of the reduced-order models is quantified using two primary metrics:

- Relative Error on peak temperature ($\varepsilon_{\Delta T}$): Evaluates the discrepancy in predicting the peak temperature rise, defined as:

$$\varepsilon_{\Delta T}[\%] = \frac{|\Delta T_{\max,mod} - \Delta T_{\max,ref}|}{\Delta T_{\max,ref}} \times 100 \tag{31}$$

- Absolute error on peak temperature position ($\Delta x$): Measures the misalignment of the temperature peaks along the conductor, defined as:

$$\Delta x[\mathrm{m}] = |x_{\max,mod} - x_{\max,ref}| \tag{32}$$

To provide a comprehensive overview of model performance across different operating regimes, Fig. 9 visually summarizes these KPIs. The dual-axis bar chart maps the relative error on the peak temperature rise (wide transparent bars, left axis) and the absolute error on the peak temperature position (thin solid markers, right axis) for the three tested numerical models. The following sections analyze the comparative results detailed in Tables 3–5, interpreting the physical implications of the trends observed in Fig. 9 for each representative operating scenario.

### 6.1. Analysis of case 1

Table 3 and the left panel of Fig. 9 illustrate the system's behavior under standard Low-Temperature Superconductor (LTS) CICC operation at 5 K with a mild temperature increase ($\Delta T \approx 2$ K).

To fully address the reliability of the simplified formulations, the analysis explicitly compares the compressible and incompressible variants. The results clearly demonstrate that accounting for fluid compressibility significantly improves the quality and reliability of the predictions at 5 K. While the relative errors in the peak temperature rise remain similar for the compressible and incompressible formulations, the corresponding spatial errors differ markedly. For instance, at 150 s, the incompressible AD1 and AD2 models exhibit a severe spatial drift, accumulating up to 11.0 m of spatial error. In contrast, by simply enabling the lumped compressibility formulation, the spatial error is tightly restricted to under 1.5 m. The PA model performs poorly regardless of compressibility, confirming that entirely removing thermal diffusion prevents the natural smoothing of the temperature profile.

**Table 3**
Comparison of the predicted peak temperature rise ($\Delta T_{\max}$), peak position ($x_{\max}$), and corresponding KPIs for Case 1.

| Time [s] | Model | Comp. | $\mathbf{\Delta T_{max}}$ [K] | $\boldsymbol{\varepsilon_{\Delta T}}$ [%] | $\mathbf{x_{max}}$ [m] | $\mathbf{\Delta x}$ [m] |
|---|---|---|---|---|---|---|
| 100 | REF | Y | 1.47 | – | 71.0 | – |
| | AD1 | Y | 1.41 | 3.49% | 72.5 | 1.5 |
| | AD1 | N | 1.42 | 3.05% | 73.0 | 2.0 |
| | AD2 | Y | 1.41 | 3.74% | 73.5 | 2.5 |
| | AD2 | N | 1.42 | 3.28% | 73.5 | 2.5 |
| | PA | Y | 1.85 | 25.93% | 30.0 | 41.0 |
| | PA | N | 1.85 | 25.93% | 30.0 | 41.0 |
| 125 | REF | Y | 1.43 | – | 86.5 | – |
| | AD1 | Y | 1.41 | 1.63% | 88.0 | 1.5 |
| | AD1 | N | 1.41 | 1.56% | 92.5 | 6.0 |
| | AD2 | Y | 1.40 | 1.82% | 88.5 | 2.0 |
| | AD2 | N | 1.41 | 1.72% | 93.5 | 7.0 |
| | PA | Y | 1.85 | 29.35% | 49.0 | 37.5 |
| | PA | N | 1.85 | 29.55% | 61.5 | 25.0 |
| 150 | REF | Y | 1.41 | – | 102.0 | – |
| | AD1 | Y | 1.40 | 1.00% | 103.0 | 1.0 |
| | AD1 | N | 1.40 | 1.29% | 112.0 | 10.0 |
| | AD2 | Y | 1.40 | 1.17% | 103.5 | 1.5 |
| | AD2 | N | 1.39 | 1.43% | 113.0 | 11.0 |
| | PA | Y | 1.85 | 30.91% | 65.0 | 37.0 |
| | PA | N | 1.86 | 31.45% | 87.0 | 15.0 |

### 6.2. Analysis of case 2

Table 4 and the central panel of Fig. 9 present the results for a more severe transient at 5 K, characterized by a higher temperature rise ($\Delta T \approx 8$ K). As the thermal load increases, the localized thermal expansion of helium becomes the dominant physical mechanism, driving strong velocity variations.

**Table 4**
Comparison of the predicted peak temperature rise ($\Delta T_{\max}$), peak position ($x_{\max}$), and corresponding KPIs for Case 2.

| Time [s] | Model | Comp. | $\Delta T_{\max}$ [K] | $\varepsilon_{\Delta T}$ [%] | $x_{\max}$ [m] | $\Delta x$ [m] |
|---|---|---|---|---|---|---|
| 100 | REF | Y | 7.25 | – | 68.0 | – |
| | AD1 | Y | 7.27 | 0.27% | 70.0 | 2.0 |
| | AD1 | N | 7.40 | 1.98% | 70.5 | 2.5 |
| | AD2 | Y | 7.44 | 2.52% | 70.5 | 2.5 |
| | AD2 | N | 7.59 | 4.57% | 71.0 | 3.0 |
| | PA | Y | 9.24 | 27.37% | 30.0 | 38.0 |
| | PA | N | 9.24 | 27.37% | 30.0 | 38.0 |
| 125 | REF | Y | 7.13 | – | 74.5 | – |
| | AD1 | Y | 7.22 | 1.20% | 75.5 | 1.0 |
| | AD1 | N | 7.21 | 1.03% | 82.0 | 7.5 |
| | AD2 | Y | 7.41 | 3.96% | 75.5 | 1.0 |
| | AD2 | N | 7.54 | 5.69% | 82.0 | 7.5 |
| | PA | Y | 9.29 | 30.30% | 36.5 | 38.0 |
| | PA | N | 9.35 | 31.05% | 41.5 | 33.0 |
| 150 | REF | Y | 7.05 | – | 80.5 | – |
| | AD1 | Y | 7.16 | 1.55% | 81.0 | 0.5 |
| | AD1 | N | 7.01 | 0.57% | 95.5 | 15.0 |
| | AD2 | Y | 7.39 | 4.79% | 81.0 | 0.5 |
| | AD2 | N | 7.49 | 6.20% | 93.5 | 13.0 |
| | PA | Y | 9.32 | 32.16% | 41.5 | 39.0 |
| | PA | N | 9.43 | 33.68% | 51.0 | 29.5 |

**Table 5**
Comparison of the predicted peak temperature rise ($\Delta T_{\max}$), peak position ($x_{\max}$), and corresponding KPIs for Case 3.

| Time [s] | Model | Comp. | $\Delta T_{\max}$ [K] | $\varepsilon_{\Delta T}$ [%] | $x_{\max}$ [m] | $\Delta x$ [m] |
|---|---|---|---|---|---|---|
| 100 | REF | Y | 10.08 | – | 54.5 | – |
| | AD1 | Y | 10.10 | 0.22% | 54.5 | 0.0 |
| | AD1 | N | 10.10 | 0.20% | 54.0 | 0.5 |
| | AD2 | Y | 10.10 | 0.23% | 51.5 | 3.0 |
| | AD2 | N | 10.10 | 0.21% | 51.0 | 3.5 |
| | PA | Y | 10.66 | 5.76% | 30.0 | 24.5 |
| | PA | N | 10.66 | 5.76% | 30.0 | 24.5 |
| 200 | REF | Y | 10.05 | – | 57.0 | – |
| | AD1 | Y | 10.07 | 0.23% | 57.5 | 0.5 |
| | AD1 | N | 10.07 | 0.22% | 57.5 | 0.5 |
| | AD2 | Y | 10.11 | 0.69% | 56.0 | 1.0 |
| | AD2 | N | 10.11 | 0.69% | 56.0 | 1.0 |
| | PA | Y | 10.76 | 7.11% | 38.5 | 18.5 |
| | PA | N | 10.76 | 7.12% | 38.5 | 18.5 |
| 300 | REF | Y | 9.91 | – | 64.0 | – |
| | AD1 | Y | 9.99 | 0.72% | 64.0 | 0.0 |
| | AD1 | N | 9.98 | 0.67% | 64.5 | 0.5 |
| | AD2 | Y | 10.12 | 2.10% | 62.5 | 1.5 |
| | AD2 | N | 10.12 | 2.11% | 63.0 | 1.0 |
| | PA | Y | 10.83 | 9.23% | 45.5 | 18.5 |
| | PA | N | 10.83 | 9.25% | 46.0 | 18.0 |

In this scenario, retaining compressibility becomes essential. While the compressible AD1 and AD2 models closely reproduce the thermal-wave position ($\Delta x \leq 2.5$ m), the incompressible counterparts show substantially larger spatial deviations. At $t = 150$ s, bypassing the mass conservation equation causes the incompressible AD1 model to misplace the peak temperature by 15.0 m. This confirms that the simplified models can only function reliably at 5 K if they inherently account for compressibility effects.

### 6.3. Analysis of case 3

Table 5 and the right panel of Fig. 9 detail the performance in the HTS operating regime at 20 K. The dominant physics shift from fluid dynamics to the heat capacity of the solids and axial thermal conduction.

In sharp contrast to the 5 K scenarios, the performance of the simplified models at 20 K remains virtually unchanged regardless of whether compressibility is included or completely neglected. At $t = 300$ s, the compressible AD1 model yields a spatial error of 0.0 m, while the incompressible version yields an almost identical 0.5 m. Under the investigated conditions at 20 K, helium exhibits a much weaker thermo-hydraulic response to heating than in the 5 K regime, and compressibility-induced variations in the flow field become secondary. Consequently, neglecting compressibility introduces only minor deviations in the predicted thermal response.

The quantitative results confirm the good performance of AD2, which substantially reduces computational complexity while retaining accurate predictions of the selected KPIs, particularly for HTS conductors operating at 20 K. Conversely, the PA model is inadequate for accurate CICC transient analysis across all tested scenarios.

A useful interpretation of the different model performances can be obtained by comparing the characteristic times associated with the two dominant heat transport mechanisms, namely longitudinal advection and axial thermal diffusion. These are defined as

$$\tau_{\mathrm{adv}} = \frac{L_{\mathrm{th}}}{u_{\mathrm{eq}}}, \qquad \tau_{\mathrm{diff}} = \frac{L_{\mathrm{th}}^2}{\alpha_{\mathrm{eq}}}, \tag{33}$$

where $u_{\mathrm{eq}}$ is the equivalent advection velocity, $L_{\mathrm{th}}$ is the characteristic axial extent of the thermal disturbance, and $\alpha_{\mathrm{eq}}$ is the equivalent thermal diffusivity of the conductor. The corresponding transport quantities are summarized in Table 6. These characteristic times can then be directly compared with the heating duration, $\tau_{\mathrm{load}} = 100$ s, providing a physically intuitive interpretation of the model's behavior.

During the heating phase ($\tau_{\mathrm{load}} = 100$ s), the characteristic advection time is comparable to or shorter than the heating duration for the two 5 K cases, whereas the characteristic diffusion time is one to two orders of magnitude larger.

The characteristic transport lengths further clarify the different roles of advection and diffusion. During the 100 s heating phase, advection transports the thermal disturbance over approximately 60 m in the two 5 K cases and about 10 m at 20 K, whereas diffusion redistributes heat over only 5 m and 2.5 m, respectively. Thus, advection governs the overall propagation of the thermal disturbance, while diffusion primarily controls the local spreading and smoothing of the thermal front. This explains the poor performance of the PA model. By neglecting diffusion, PA suppresses the local redistribution of heat, producing artificially sharp temperature fronts and inaccurate predictions of the peak location. These discrepancies are particularly pronounced at 5 K, where compressibility further enhances the asymmetry of the thermal wave. The advection–diffusion models (AD1 and AD2), on the other hand, retain both leading-order transport mechanisms. Their excellent agreement with the REF model confirms that both mechanisms are required to accurately reproduce slow thermal transients in HTS CICCs. From a physical perspective, the transition from 5 K to 20 K should not be interpreted as a transition from diffusion-dominated to advection-dominated behavior. Rather, it reflects a shift in the dominant thermal inertia and in the role of compressibility. At 20 K, helium expansion becomes secondary and the thermal response is increasingly governed by the solid components, while axial diffusion remains essential to correctly reproduce the spatial structure of the thermal field. These observations explain why, within the slow-transient regime considered here, AD2 represents the minimum physically consistent formulation among the models investigated.

The present analysis also provides indications on the expected range of validity of the proposed reduced-order formulations. The reduction strategy relies on three fundamental assumptions: (i) a clear separation between the characteristic timescale of the transient and the thermal equilibration timescale within the conductor cross-section, (ii) the predominance of one-dimensional axial transport mechanisms, and (iii) operating conditions for which advection and diffusion remain the dominant contributions to the thermal evolution. Consequently, the proposed AD2 formulation is expected to remain valid for slow thermal transients the characteristic timescale of which is significantly larger than the characteristic thermal diffusion time of the solid domain and for operating conditions similar to those investigated in this work.

**Table 6**
Characteristic transport quantities employed to interpret the thermal transient in the AD2 model. The characteristic thermal disturbance length is taken as $L_{\text{th}} = 37$ m, while the heating duration is $\tau_{\text{load}} = 100$ s.

| Quantity | Definition | Expression | Case 1 | Case 2 | **Case 3** |
|---|---|---|---|---|---|
| $u_{\text{eq}}$ [m/s] | Equivalent advection velocity | $\frac{u_{\text{eff}}}{c_s + c_{\text{He}}}$ | $6.39 \times 10^{-1}$ | $6.02 \times 10^{-1}$ | $1.04 \times 10^{-1}$ |
| $\alpha_{\text{eq}}$ [$m^2$/s] | Equivalent thermal diffusivity | $\frac{\alpha_{\text{eff}}}{c_s + c_{\text{He}}}$ | $2.34 \times 10^{-1}$ | $3.04 \times 10^{-1}$ | $6.15 \times 10^{-2}$ |
| $\tau_{\text{adv}}$ [s] | Characteristic advection time | $\frac{L_{\text{th}}}{u_{\text{eq}}}$ | 57.9 | 61.5 | 357.0 |
| $\tau_{\text{diff}}$ [s] | Characteristic diffusion time | $\frac{L_{\text{th}}^2}{\alpha_{\text{eq}}}$ | $5.85 \times 10^3$ | $4.50 \times 10^3$ | $2.23 \times 10^4$ |
| $L_{\text{adv}}$ [m] | Advection length during heating | $u_{\text{eq}}\tau_{\text{load}}$ | 63.9 | 60.2 | 10.4 |
| $L_{\text{diff}}$ [m] | Diffusion length during heating | $\sqrt{\alpha_{\text{eq}}\tau_{\text{load}}}$ | 4.84 | 5.51 | 2.48 |

Conversely, the accuracy of the model may deteriorate for very fast transients, strongly localized heat deposition events, or situations in which multidimensional effects become relevant.

Similarly, the reduced compressibility treatment remains appropriate as long as the flow remains in the low-Mach-number regime and pressure-driven effects are primarily associated with thermal expansion rather than with strong hydrodynamic transients.

The identification of these validity limits is particularly important because it highlights that the proposed model reduction is not purely mathematical, but rather derives from the hierarchy of physical mechanisms governing HTS CICC operation around 20 K.

## 7. Conclusions

This work investigates the minimum level of thermo-hydraulic model complexity required to accurately reproduce slow thermal transients in HTS cable-in-conduit conductors operating around 20 K.

A complete thermal-hydraulic reference model (REF) was systematically compared with progressively simplified formulations: a coupled advection–diffusion model retaining separate energy balances for helium and the solid domains (AD1), a single-equation advection–diffusion model for the mean conductor temperature (AD2), and a pure-advection approximation (PA). Particular attention was devoted to the role of helium compressibility and to the change in the dominant physical mechanisms occurring between the low-temperature regime (5 K) and the HTS operating regime (20 K).

The results demonstrate that the transition from 4.5 K to 20 K is not merely a change in operating temperature, but rather a transition between two fundamentally different thermo-hydraulic regimes. At 5 K, the transient response is strongly governed by helium compressibility and by the highly non-linear behavior of supercritical helium. In this regime, simplified formulations remain accurate only if compressibility effects are properly retained through reduced-order descriptions of the fluid dynamics. Conversely, at 20 K, helium behaves essentially as a gas and the dominant thermal inertia shifts toward the solid components of the conductor. Under these conditions, the transient evolution becomes primarily governed by advection and axial thermal diffusion, while pressure effects become secondary. As a consequence, reduced-order advection–diffusion models accurately reproduce both the temperature peak and the spatial evolution of the thermal profile with limited errors compared to the complete thermal-hydraulic formulation.

Among the simplified approaches considered, the single-equation advection–diffusion model (AD2) provides the best compromise between physical consistency and computational simplicity. Despite relying on a strongly reduced mathematical structure, the model preserves the dominant transient physics in the HTS regime and remains quantitatively accurate for the operating conditions investigated. At the same time, it achieves reductions in computational cost exceeding one order of magnitude compared to the complete thermal-hydraulic formulation, making it particularly attractive for design studies, parametric analyses, and system-level simulations. By contrast, the pure advection model fails to reproduce the transient dynamics in the low-temperature regime and remains unable to correctly capture the spatial spreading of the thermal profile even at 20 K, highlighting the essential role of diffusive mechanisms in CICC thermal transients. The identification of AD2 as the minimum physically consistent formulation is, however, linked to the slow-transient regime considered in the present analysis. In particular, the characteristic load duration of approximately 100 s remains significantly larger than the relevant thermal equilibration timescales within the conductor. If this separation of timescales is progressively reduced, the single-temperature and quasi-steady assumptions underlying AD2 may no longer remain adequate, and validation against the complete REF formulation becomes necessary.

More generally, the present work shows that the reduction of thermo-hydraulic models for HTS CICCs can be performed consistently only after identifying the hierarchy of the relevant physical mechanisms in the considered operating regime. The proposed methodology therefore provides not only a reduced-order modeling strategy, but also a physics-based framework for determining which processes can be neglected and which must be retained when moving from LTS to HTS operating conditions.

Future developments will focus on extending the present approach to faster transients, more complex conductor layouts, and coupled magnet-network simulations, as well as on the validation of the reduced-order formulations against experimental data.

## CRediT authorship contribution statement

**Laura Savoldi:** Writing – original draft, Validation, Supervision, Resources, Project administration, Methodology, Funding acquisition, Formal analysis, Conceptualization. **Martina Casciello:** Writing – review & editing, Software, Formal analysis. **Mattia Gaspare Ciccarese:** Writing – original draft, Visualization, Validation, Software, Investigation, Formal analysis, Data curation. **Mattia De Stasio:** Writing – review & editing, Software, Formal analysis. **Michele Prisco:** Writing – original draft, Visualization, Validation, Software, Investigation, Formal analysis, Data curation. **Andrea Tosin:** Writing – review & editing, Supervision, Formal analysis, Conceptualization.

## Declaration of Generative AI and AI-assisted technologies in the writing process

During the preparation of this work, the authors used ChatGPT to improve the manuscript's readability. The authors reviewed and edited the content and take full responsibility for the publication.

## Declaration of competing interest

The authors declare that they have no known competing financial interests or personal relationships that could have appeared to influence the work reported in this paper.

## Appendix A. Derivation of the lumped compressible flow equation

### A.1. Mathematical formulation of the compressible flow

Starting from the one-dimensional mass conservation equation introduced in Section 3.5, the formula can be expressed in terms of mass flow rate:

$$A_{\mathrm{He}}\frac{\partial \rho_{\mathrm{He}}}{\partial t}+\frac{\partial \dot{m}}{\partial x}=0, \tag{A.1}$$

where $A_{\mathrm{He}}$ is the helium cross-sectional area, $\rho_{\mathrm{He}}$ is the fluid density, and $\dot{m}=\rho_{\mathrm{He}}vA_{\mathrm{He}}$ is the mass flow rate. To determine the velocity variations along the conductor driven by thermal expansion, the spatial derivative of the mass flow rate is isolated:

$$\frac{\partial \dot{m}}{\partial x}=-A_{\mathrm{He}}\frac{\partial \rho_{\mathrm{He}}}{\partial t}. \tag{A.2}$$

This expression dictates that if the fluid heats up and its density decreases, the right-hand side becomes positive, requiring the local mass flow rate and velocity to increase. By integrating this expression along the spatial coordinate from the cable inlet ($x=0$) to a generic position $x$, the exact mass flow rate at any location is obtained:

$$\dot{m}(x)=\dot{m}_{\mathrm{in}}-A_{\mathrm{He}}\int_0^x\frac{\partial \rho_{\mathrm{He}}}{\partial t}\,dx', \tag{A.3}$$

where the inlet boundary condition is introduced as the prescribed, constant mass flow rate $\dot{m}_{\mathrm{in}}=\rho_{\mathrm{He}}(0)v(0)A_{\mathrm{He}}$. The local fluid velocity $v(x)$ can then be explicitly computed as:

$$v(x)=\frac{1}{\rho_{\mathrm{He}}(x)A_{\mathrm{He}}}\left(\dot{m}_{\mathrm{in}}-A_{\mathrm{He}}\int_0^x\frac{\partial \rho_{\mathrm{He}}}{\partial t}\,dx'\right). \tag{A.4}$$

### A.2. Numerical discretization

To implement this reduced-order approach numerically, the continuous equations are discretized over a spatial grid of nodes. The local density derivative with respect to time at node $i$ is approximated using a first-order backward finite difference (Implicit Euler method):

$$\left(\frac{\partial \rho_{\mathrm{He}}}{\partial t}\right)_i\approx\frac{\rho_{\mathrm{He},i}^{n+1}-\rho_{\mathrm{He},i}^{n}}{\Delta t}, \tag{A.5}$$

where $n$ and $n+1$ denote the previous and current time steps, respectively. The spatial integration is then performed numerically using a cumulative sum along the grid with a step size of $\Delta x$:

$$\dot{m}_i=\dot{m}_{\mathrm{in}}-\sum_{j=1}^{i}A_{\mathrm{He}}\left(\frac{\rho_{\mathrm{He},j}^{n+1}-\rho_{\mathrm{He},j}^{n}}{\Delta t}\right)\Delta x. \tag{A.6}$$

Finally, the local velocity $v_i$ is explicitly extracted at each node based on the continuously updated thermodynamic state:

$$v_i=\frac{\dot{m}_i}{\rho_{\mathrm{He},i}^{n+1}A_{\mathrm{He}}}. \tag{A.7}$$

This explicit calculation methodology ensures excellent numerical stability. By computing the fluid dynamics entirely from the thermodynamic state of the density, the model successfully avoids introducing numerically unstable pressure oscillations while fully preserving the physics of helium thermal expansion.

## Appendix B. Derivation and truncation of the single-equation advection–diffusion model

This appendix outlines the derivation of the single-equation model adopted for AD2, starting from a coupled solid–fluid thermal system. The full derivation naturally leads to a diffusion–dispersion equation containing higher-order spatial derivatives. However, in accordance with the objective of identifying a minimum-complexity model, these higher-order contributions are consistently neglected, leading to a reduced advection–diffusion formulation.

Starting from the coupled solid–fluid energy equations (reported in the main text), the system is rewritten in terms of the mean temperature and temperature difference:

$$T_{\mathrm{mean}}=\frac{T_s+T_{He}}{2},\qquad \Delta T=T_s-T_{He}. \tag{B.1}$$

This transformation allows the system to be recast into two coupled equations governing the evolution of $T_{\mathrm{mean}}$ and $\Delta T$.

By summing and subtracting the original equations, one obtains:

- a mean-temperature equation, containing both $T_{\mathrm{mean}}$ and $\Delta T$;
- a difference equation, governing the evolution of $\Delta T$.

To obtain a reduced formulation, a quasi-steady assumption is introduced for the temperature difference:

$$\frac{\partial \Delta T}{\partial t}\approx 0, \tag{B.2}$$

reflecting the fact that the solid–fluid temperature gap relaxes on a faster timescale than the mean thermal field.

Assuming a low-order closure for the temperature difference, the temperature difference is approximated as a function of the first two spatial derivatives of the mean temperature:

$$\Delta T\approx A\frac{\partial^2 T_{\mathrm{mean}}}{\partial x^2}+B\frac{\partial T_{\mathrm{mean}}}{\partial x}. \tag{B.3}$$

This closure retains the dominant contribution of solid–fluid thermal disequilibrium while neglecting higher-order effects. The coefficients $A$ and $B$ are obtained by substituting this expression into the difference equation and matching terms of equal derivative order, yielding:

$$B=\frac{u}{h_{\mathrm{He,Cu}}P_{\mathrm{He,Cu}}\left(\frac{1}{c_{He}}+\frac{1}{c_s}\right)}, \tag{B.4}$$

$$A=\frac{A_s k_s}{h_{\mathrm{He,Cu}}P_{\mathrm{He,Cu}}\left(\frac{c_s}{c_{He}}+1\right)}-\frac{u^2}{2h_{\mathrm{He,Cu}}^2P_{\mathrm{He,Cu}}^2\left(\frac{1}{c_{He}}+\frac{1}{c_s}\right)^2}. \tag{B.5}$$

Substituting the closure for $\Delta T$ into the mean-temperature equation leads to a reduced equation of the form:

$$(c_s+c_{He})\frac{\partial T_{\mathrm{mean}}}{\partial t}+c_{He}u\frac{\partial T_{\mathrm{mean}}}{\partial x}=D_2\frac{\partial^2 T_{\mathrm{mean}}}{\partial x^2}+D_3\frac{\partial^3 T_{\mathrm{mean}}}{\partial x^3}+D_4\frac{\partial^4 T_{\mathrm{mean}}}{\partial x^4}+q', \tag{B.6}$$

where $D_2$, $D_3$, and $D_4$ are coefficients arising from the solid–fluid coupling.

The second-order term represents effective diffusion, while the third- and fourth-order terms correspond to dispersive corrections associated with asymmetry and smoothing of the thermal profile.

Although the higher-order terms arise naturally from the derivation, they are not retained in the operational AD2 model.

This truncation is consistent with both the modeling assumptions and the physical regime considered. In particular, the analysis focuses on slow transients, for which the temperature field varies smoothly along the conductor and is primarily governed by advection and effective diffusion. In this regime, the third- and fourth-order derivatives provide only higher-order corrections.

Moreover, the closure adopted for $\Delta T$ is itself a low-order approximation, constructed to retain only the dominant dependence on the first and second spatial derivatives of $T_{\mathrm{mean}}$. Retaining higher-order terms in the final equation would therefore be inconsistent with the objective of constructing a reduced-order model.

Finally, including third- and fourth-order derivatives would significantly increase the mathematical and numerical complexity of the model, requiring additional boundary conditions and more restrictive discretization schemes, without a corresponding improvement in accuracy for the class of transients considered.

Accordingly, the AD2 model is written by retaining only the dominant terms:

$$(c_s + c_{He})\frac{\partial T_{\text{mean}}}{\partial t} + u_{\text{eff}}\frac{\partial T_{\text{mean}}}{\partial x} = \alpha_{\text{eff}}\frac{\partial^2 T_{\text{mean}}}{\partial x^2} + q' + q'_{\text{fric}}, \tag{B.7}$$

where

$$u_{\text{eff}} = c_{p,\text{He}}\dot{m}, \qquad \alpha_{\text{eff}} = A_s k_s + \frac{1}{2}c_{He}uB. \tag{B.8}$$

The neglected higher-order terms should therefore be interpreted as dispersive corrections that are consistently excluded in order to obtain a computationally efficient reduced-order model.

## Appendix C. Initialization of the pure advection model

In the pure advection (PA) model, the initial temperature distribution is forced to follow a normalized trapezoidal shape $S(x)$ that mirrors the spatial distribution of the externally applied heat load. The initial temperature profile $T_{\text{mean}}(x,0)$ is expressed as a function of the baseline temperature $T_{op}$ and an unknown peak temperature rise $\Delta T_{\max}$:

$$T_{\text{mean}}(x,0) = T_{op} + \Delta T_{\max} S(x). \tag{C.1}$$

To determine $\Delta T_{\max}$, the system is assumed to be adiabatic during the heat deposition phase. Consequently, the total deposited energy $E_{tot}$ must strictly equal the overall enthalpy variation of the cable. This requires integrating the specific heat capacities along the local temperature ramp:

$$E_{tot} = \int_0^L \sum_i A_i \left( \int_{T_{op}}^{T_{\text{mean}}(x,0)} (\rho c_p)_i(T)\, dT \right) dx, \quad i \in \{\text{He}, \text{Cu}, \text{SS}\}. \tag{C.2}$$

Because the material properties are highly non-linear, this energy balance equation cannot be inverted analytically. As a result, a bisection algorithm is employed to iteratively adjust the value of $\Delta T_{\max}$ until the calculated energy variation converges to the known total deposited energy $E_{tot}$.

## Data availability

The numerical data and simulation results supporting the findings of this study are available from the corresponding author upon request.

## References


[1] Hartwig ZS, et al. The SPARC toroidal field model coil program. IEEE Trans Appl Supercond 2024;34:0600316.
[2] Li Z, Pan Z, Zhang Q, Zhu K, Zhang C, Zhang Z, Dong G, Ye Y, Yang Z. Development and construction of magnet system for world's first full high temperature superconducting tokamak. Superconductivity 2024;12:100137. https://doi.org/10.1016/j.supcon.2024.100137. https://www.sciencedirect.com/science/article/pii/S2772830724000541.
[3] CERN. The large hadron collider. 2025. https://home.cern/science/accelerators/large-hadron-collider/ [Accessed: 18 May 2026].
[4] ITER Organization. ITER; 2025 https://www.iter.org/ [Accessed: 18 May 2026].
[5] Bottura L. Modelling stability in superconducting cables. Phys C Supercond Appl 1998;310(1–4):316–26. https://doi.org/10.1016/S0921-4534(98)00482-1. https://www.scopus.com/inward/record.uri?eid=2-s2.0-0032256860&doi=10.1016S0921-4534%2898%2900482-1&partnerID=40&md5=bf59b3946bfdfd4952d3e3e7b753d485.
[6] Breschi M, Savoldi L, Cavallucci L, Bottura L. Characteristic timescales for the operation of HTS CICCs in compact fusion reactors. IEEE Trans Appl Supercond 2025;35(5):1–5. https://doi.org/10.1109/TASC.2025.3554466
[7] Bessette D, Shatil N, Zapretilina E. Simulations of the ITER toroidal field coil operation with the VINCENTA code; 2006) 795–798. https://doi.org/10.1109/TASC.2006.873258. https://www.scopus.com/inward/record.uri?eid=2-s2.0-33746640530&doi=10.1109TASC.2006.873258&partnerID=40&md5=7eaa56748a42c74bb2d7c597b4a246c8. 16 (2).
[8] Bottura L. A numerical model for the simulation of quench in the ITER magnets. J Comput Phys 1996;125:26–41.
[9] Bottura L, Rosso C, Breschi M. A general model for thermal, hydraulic and electric analysis of superconducting cables. Cryogenics 2000;40(8):617–26, 4th Workshop on Computation of Thermal Hydraulic Transients in Superconductors. https://doi.org/10.1016/S0011-2275(01)00019-4. https://www.sciencedirect.com/science/article/pii/S0011227501000194.
[10] CryoSoft. SuperMagnet user's guide; 2007. http://www.cern.ch/botturl/CryoSoft/manuals/SuperMagnet_2.0.pdf., Version 1.0, CryoSoft, Louisville, CO, USA.
[11] Lacroix B, Le Coz Q, Louzguiti A, Nicollet S, Torre A, Zani L, Barjhoux P, Bonne F, Nunio F. Latest developments of OLYMPE platform for optimizing design of fusion cryomagnetic systems. IEEE Trans Appl Supercond 2024;34(5):1–5. https://doi.org/10.1109/TASC.2024.3355350
[12] Zanino R, De Palo S, Bottura L. A two-fluid code for the thermohydraulic transient analysis of CICC superconducting magnets. J Fusion Energy 1995;14(1):25–40. https://doi.org/10.1007/BF02214031
[13] Savoldi L, Zanino R. M&M: multi-conductor mithrandir code for the simulation of thermal-hydraulic transients in superconducting magnets. Cryogenics 2000;40(3):179–89. https://doi.org/10.1016/S0011-2275(00)00027-8
[14] Savoldi Richard L, Casella F, Fiori B, Zanino R. The 4C code for the cryogenic circuit conductor and coil modeling in ITER. Cryogenics 2010;50(3):167–76, CHATS on Applied Superconductivity Workshop 2008. https://doi.org/10.1016/j.cryogenics.2009.07.008. https://www.sciencedirect.com/science/article/pii/S0011227509001118.
[15] Savoldi L, Bonifetto R, Casella F, Ferrari ML. Thermal-hydraulic analysis of superconducting cables for energy applications with a novel open object-oriented software: OPENSC2. Cryogenics 2022;124:103457. https://doi.org/10.1016/j.cryogenics.2022.103457
[16] Duchateau J, Fillunger H, Fink S, Heller R, Hertout P, Libeyre P, Maix R, Marinucci C, Martinez A, Meyder R, Nicollet S, Raff S, Ricci M, Savoldi L, Ulbricht A, Wuechner F, Zahn G, Zanino R. Test program preparations of the ITER toroidal field model coil (TFMC). Fusion Eng Des 2001;58-59:147–51. https://doi.org/10.1016/S0920-3796(01)00570-1. https://www.sciencedirect.com/science/article/pii/S0920379601005701.
[17] Savoldi L, Zanino R, Marchese V, Martovetsky N, Suesser M, Ulbricht A, Wuechner F, Zahn G. First measurement of the current sharing temperature at 80 kA in the ITER toroidal field model coil (TFMC). IEEE Trans Appl Supercond 2002;12(1):635–8. https://doi.org/10.1109/TASC.2002.1018482
[18] Heller R, Duchateau JL, Nicollet S, Prat F. Numerical evaluation of the quench behaviour of the ITER toroidal field model coil. In: Kittel P, editor. Advances in cryogenic engineering, Vol. 43 of advances in cryogenic engineering. Boston, MA: Springer; 1998. p. 193–200. https://doi.org/10.1007/978-1-4757-9047-4_21
[19] Zanino R, Mitchell N, Richard L. Analysis and interpretation of the full set (2000–2002) of TCS tests in conductor 1A of the ITER central solenoid model coil. Cryogenics 2003;43(3):179–97. https://doi.org/10.1016/S0011-2275(03)00035-3. https://www.sciencedirect.com/science/article/pii/S0011227503000353.
[20] Savoldi Richard L, Bonifetto R, Chu Y, Kholia A, Park SH, Lee HJ, Zanino R. 4C code analysis of thermal–hydraulic transients in the KSTAR PF1 superconducting coil. Cryogenics 2013;53:37–44. https://doi.org/10.1016/j.cryogenics.2012.04.015. https://www.sciencedirect.com/science/article/pii/S0011227512000860.
[21] Lee HJ, Chu Y, Kim KP, Kim HW, Park K. Effect of flow imbalance on the operational performance of the KSTAR PF1UL magnets. Fusion Eng Des 2021;172:112770. https://doi.org/10.1016/j.fusengdes.2021.112770. https://www.sciencedirect.com/science/article/pii/S0920379621005469.
[22] Zanino R, Bonifetto R, Bottero U, Li J, Qian J, Hu L, Gao X, Savoldi Richard L, Wu Y. Application of the 4C code to the thermal–hydraulic analysis of the CS superconducting magnets in EAST. Cryogenics 2014;63:255–62. https://doi.org/10.1016/j.cryogenics.2014.06.004. https://www.sciencedirect.com/science/article/pii/S0920379601005701.
[23] Zappatore A, Bonifetto R, Bruzzone P, Corato V, Zenobio AD, Savoldi L, Sedlak K, Turtù S, Zanino R. Performance analysis of the NbTi PF coils for the EU DEMO fusion reactor. IEEE Trans Appl Supercond 2018;28(4):1–5. https://doi.org/10.1109/TASC.2018.2793462
[24] Savoldi L, Brighenti A, Bonifetto R, Corato V, Muzzi L, Turtù S, Zanino R. Performance analysis of a graded winding pack design for the EU DEMO TF coil in normal and off-normal conditions. Fusion Eng Des 2017;124:45–8, Proceedings of the 29th Symposium on Fusion Technology (SOFT-29) Prague, Czech Republic, September 5–9, 2016. https://doi.org/10.1016/j.fusengdes.2017.05.107. https://www.sciencedirect.com/science/article/pii/S0920379617306646.
[25] Guarino R, Lewandowska M, Dembkowska A, Bykovskiy N, Sarasola X, Sedlak K. Thermal-hydraulic analysis of alternative cable-in-conduit conductors for the European DEMO hybrid central solenoid. Fusion Eng Des 2023;187:113368. https://doi.org/10.1016/j.fusengdes.2022.113368. https://www.sciencedirect.com/science/article/pii/S0920379622003581.
[26] Lewandowska M, Dembkowska A, Nes T. Thermal-hydraulic and quench analysis of conductors for the EU-DEMO LAR coil. IEEE Trans Appl Supercond 2026;36(5):1–5. https://doi.org/10.1109/TASC.2026.3676044
[27] Wen X, Bonifetto R, Li J, Zanino R, Wu Y, Gao X. Thermal-hydraulic simulation of the CFETR TF coil operation during a plasma scenario: gandalf-fluent and 4C code-to-code comparison. Fusion Eng Des 2023;197:114033. https://doi.org/10.1016/j.fusengdes.2023.114033. https://www.sciencedirect.com/science/article/pii/S0920379623006130.
[28] Savoldi Richard L, Bonifetto R, Bottero U, Foussat A, Mitchell N, Seo K, Zanino R. Analysis of the effects of the nuclear heat load on the ITER TF magnets temperature margin. IEEE Trans Appl Supercond 2014;24(3):1–4. https://doi.org/10.1109/TASC.2013.2280720

[29] Zanino R, Bessette D, Richard LS. Quench analysis of an ITER TF coil. Fusion Eng Des 2010;85(5):752–60. https://doi.org/10.1016/j.fusengdes.2010.04.056. https://www.sciencedirect.com/science/article/pii/S0920379610001973.

[30] Wen X, Li J, Sang A, Ren Y, Liu X, Gao X. Quench analysis of the CFETR TF coil using the gandalf code. IEEE Trans Appl Supercond 2021;31:1–5. https://api.semanticscholar.org/CorpusID:232061707.

[31] Dembkowska A, Lewandowska M, Sarasola X, Sedlak K. Quench analysis of the DEMO CS1 coil. Cryogenics 2020;112:103194. https://doi.org/10.1016/j.cryogenics.2020.103194. https://www.sciencedirect.com/science/article/pii/S001122752030196X.

[32] Huang Y, Abdel Maksoud W, Baudouy B, Ciazynski D, Decool P, Genini L, Lacroix B, Le Coz Q, Nicollet S, Nunio F, Torre A, Vallcorba R, Zani L. Numerical modeling of the quench propagation phase in the JT-60SA TF coils. IEEE Trans Appl Supercond 2018;28(3):1–5. https://doi.org/10.1109/TASC.2018.2799176

[33] Savoldi L, Bonifetto R, Pedroni N, Zanino R. Analysis of a protected loss of flow accident (LOFA) in the ITER TF coil cooling circuit. IEEE Trans Appl Supercond 2018;28(3):1–9. https://doi.org/10.1109/TASC.2017.2786688

[34] Gorit Q, Lacroix B, Louzguiti A, Nicollet S, Topin F, Torre A. A simplified 1-D quench model for preliminary prediction applied to JT-60SA toroidal field coil. Fusion Eng Des 2023;191:113571. https://doi.org/10.1016/j.fusengdes.2023.113571. https://www.sciencedirect.com/science/article/pii/S0920379623001552.

[35] Bottura L, et al. A “20 T at 20 k” model coil for the muon collider target solenoid and fusion applications. IEEE Trans Appl Supercond 2026;36(3):1–8. https://doi.org/10.1109/tasc.2026.3656861